Multiplexed Sensing of Magnetic Field and Temperature in Real Time Using a Nitrogen-Vacancy Ensemble in Diamond

Jeong Hyun Shim,[1,2,*] Seong-Joo Lee,[1] Santosh Ghimire,[1] Ju Il Hwang,[3] Kwang-Geol Lee,[3] Kiwoong Kim,[4] Matthew J. Turner,[5,6,7] Connor A. Hart,[5,6,7] Ronald L. Walsworth,[5,6,7] and Sangwon Oh[1,†]

[1] *Korean Research Institute of Standards and Science, Daejeon 34113, Republic of Korea*
[2] *Department of Medical Physics, University of Science and Technology, Daejeon 34113, Republic of Korea*
[3] *Department of Physics, Hanyang University, Seoul 04763, Republic of Korea*
[4] *Department of Physics, Chungbuk National University, Cheongju 28644, Republic of Korea*
[5] *Department of Physics, University of Maryland, College Park, Maryland 20742, USA*
[6] *Department of Electrical Engineering and Computer Science, University of Maryland, College Park, Maryland 20742, USA*
[7] *Quantum Technology Center, University of Maryland, College Park, Maryland 20742, USA*

(Received 25 April 2021; revised 3 August 2021; accepted 17 November 2021; published 7 January 2022)

The nitrogen-vacancy (N-V) defect in diamond is a versatile quantum sensor, being able to measure physical quantities such as magnetic field, electric field, temperature, and pressure. In the present work, we demonstrate multiplexed sensing of magnetic field and temperature using a N-V ensemble in diamond. The dual-frequency-driving technique we employ is based on frequency-division multiplexing, which enables the sensing of both measurables in real time. The pair of N-V resonance frequencies for dual-frequency driving must be selected to avoid coherent population trapping of N-V spin states. With enhanced optical collection efficiency higher than 50% and a type 1b diamond crystal with a natural abundance of ^{13}C spins, we achieve sensitivities of about 70 pT/$\sqrt{\text{Hz}}$ and 25 μK/$\sqrt{\text{Hz}}$ simultaneously. We demonstrate a high isolation factor of 34 dB in the N-V thermometry signal against the magnetic field; and we provide a theoretical description for the isolation factor. This work paves the way for extending the application of N-V diamond sensors into more demanding conditions.

DOI: 10.1103/PhysRevApplied.17.014009

I. INTRODUCTION

An ensemble of negatively charged nitrogen-vacancy (N-V) defect in diamond can provide a broadband magnetic field sensitivity in the picotesla range, depending on the instrument details [1–8]. For such quantum diamond magnetometers, precise measurement of the N-V spin resonance frequencies is essential. The energy levels of N-V spin states, however, depend on other physical quantities [9] as well, such as temperature [10], electric field [11], strain [12], and pressure [13]. Thus, when exploited as a magnetometer, N-V spins need to be isolated from variations of other quantities to read the correct value of the magnetic field. Under ambient conditions, where the effects of electric fields and pressure are typically negligible, distinguishing between thermal and magnetic sources is a primary challenge. In principle, the more sensitive a diamond magnetometer is, the stronger it is affected by thermal variation. In other words, a sensitive diamond magnetometer can also function as a sensitive thermometer. There have been early works demonstrating pulse sequences on N-V spins in order to operate selectively as either a magnetometer or a thermometer. For example, double quantum (DQ) sequences allow N-V spins to accumulate net phase induced by magnetic fields, while being insensitive to thermal variations [14,15]. Conversely, with magnetically insensitive sequences, such as D-Ramsey, the accumulated net phase is dominantly sensitive to temperature [16–19]. For multiplexing these measurables, continuous-wave (cw) operation has to date relied on time division, i.e., alternating quantities projected by optical readout, leading to sequential monitoring of the magnetic field and temperature with a specific time step [20–22]. Frequency-division multiplexing enables the implementation of a real-time recording of multiple quantities, because multiple frequency components can coexist in a continuously varying signal [4,23]. In this paper, we demonstrate that with dual-frequency driving [6], magnetic and thermal variations can be measured

*jhshim@kriss.re.kr
†sangwon.oh@kriss.re.kr

concurrently using a N-V diamond sensor. With enhanced optical collection efficiency (> 50%) and dual frequency driving, we achieve a magnetic field sensitivity of 70 pT/$\sqrt{\text{Hz}}$ and a temperature sensitivity of 25 μK/$\sqrt{\text{Hz}}$ simultaneously, with an isolation factor of about 34 dB, using a high-pressure–high-temperature- (HPHT) grown diamond crystal with natural ^{13}C abundance and a [NV] $\approx$ 0.5 ppm (see further information below).

II. RESULTS

A. Background

The shot-noise-limited sensitivity η_B of a N-V diamond magnetometer using continuous wave (cw) optically detected magnetic resonance (ODMR) is governed by the intrinsic properties of N-V centers and extrinsic configurations of optical detection, and can be expressed as [24,25]

$$\eta_B = \frac{\Delta f}{\frac{\gamma}{2\pi}C}\sqrt{\frac{2e}{i_{\text{ph}}}}, \tag{1}$$

where γ and e are the gyromagnetic ratio and electron charge, respectively, while Δf and C are the line width and cw ODMR contrast measured via lock-in detection. The ratio $(\Delta f/C)$ is associated with the inverse of the zero-crossing slope (α) of the lock-in detected ODMR signal, and converts the voltage noise, induced by the shot noise of the photoinduced reverse current (i_{ph}) out of a photodiode, to magnetic field noise (see Sec. S1 of the Supplemental Material [24]). Given η_B, the temperature sensitivity for the η_T is anticipated as

$$\eta_T = \frac{\gamma}{2\pi\kappa}\eta_B, \tag{2}$$

in which $\kappa = |(\partial D/\partial T)| = 74.2$ kHz/K (where D is the zero-field splitting) at room temperature [10]. Typically, the obtainable values for an optimized N-V ensemble [8] ($\Delta f = 1$ MHz, $C = 1$ %, $i_{\text{ph}} = 10$ mA) lead to sensitivities of $\eta_B \approx 20$ pT/$\sqrt{\text{Hz}}$ and $\eta_T \approx 7.6$ μK/$\sqrt{\text{Hz}}$. Although Δf and C are dependent on the pumping laser and microwave driving power, their limits are also strongly influenced by the quality of the diamond, e.g., sources of line broadening and charge trapping [8,26].

B. N-V diamond sensor

In the present work, we use a type 1b HPHT diamond crystal with a natural ^{13}C abundance and an initial neutral substitutional nitrogen (N_S^0) concentration of approximately 30 ppm (see the Appendix). N-V centers are created by electron irradiation and then annealing of the diamond sample at high temperature. After this treatment, the residual concentrations of the nitrogen (N_S^0) and N-V spins are measured via EPR to be 1.3 ppm and 0.5 ppm, respectively. (See the supplementary material for additional discussion [20].) In order to optimize i_{ph} in Eq. (1), collection optics are designed to increase the collection of the fluorescence signal from the N-V centers and to deliver it to the signal photodiode as depicted in Fig. 1(a). A half-ball lens made of a high-refractive-index material ($n \cong 2.0$, S-LAH79) is used to alleviate the light trapping inside the high-index diamond region ($n = 2.4$). Numerical calculations show that the solid angle of the photon escape cone is nearly five times as high as that without the half-ball lens; and hence the total photon collection efficiency is approximately 56% (see Sec. S2 of the Supplemental Material [24]).

C. Dual-frequency driving

The Hamiltonian for the N-V electronic spin ($S = 1$) coupled to an ^{14}N nuclear spin ($I = 1$) can be expressed as $\mathcal{H} = \text{DS}_z^2 + \gamma BS_z + A_{zz}S_zI_z - PI_z^2$ with zero-field splitting D, magnetic field B along the N-V spin orientation $(B_x, B_y = 0)$, ^{14}N quadrupole splitting P, and the hyperfine coupling A_{zz} [27]. With a static magnetic field aligned along the [111] orientation of the diamond crystal, the N-V centers parallel to the field reveal six transitions in the ODMR spectrum, as shown in Fig. 1(b). The center (f_-) of the lower-frequency triplet corresponds to $D(t) - \gamma B(t)$, while that (f_+) of the higher frequency corresponds to $D(t) + \gamma B(t)$, assuming that the zero-field splitting and the magnetic field are time-varying parameters with $D(t) = D_0 + \Delta D(t)$ and $B(t) = B_0 + \Delta B(t)$, where D_0 and B_0 are time invariant.

We employ a dual-frequency-driving scheme for multiplexed sensing of the magnetic field and the temperature. We apply two microwave signals (MW1 and MW2) that simultaneously drive the two N-V transitions centered at f_- and f_+. Both MW1 and MW2 are frequency modulated according to reference signals (Ref1 and Ref2), shown in Fig. 1(a), which are also fed into two lock-in amplifiers (LIA1 and LIA2) independently. The frequencies (f_1^R and f_2^R) and phases (ϕ_1^R and ϕ_2^R) of Ref1 and Ref2 can be adjusted depending on which quantity (magnetic field and/or temperature) is to be measured by the N-V diamond sensor. For multiplexed sensing, it is necessary to offset f_1^R from f_2^R with the difference $|f_1^R - f_2^R|$ larger than the bandwidth of either lock-in amplifier. Then, the outputs of LIA1 (S_1) and LIA2 (S_2) are given as $S_1(t) = \alpha[\Delta D(t) - \gamma\Delta B(t)]$ and $S_2(t) = \alpha[\Delta D(t) + \gamma\Delta B(t)]$, respectively, where α is the slope of the LIA output. By adding and subtracting $S_1(t)$ and $S_2(t)$, we can obtain both the magnetic field $\Delta B(t)$ and the thermal $\Delta D(t)$ variations in real time. If multiplexing is not necessary, the more common configuration is to use only a single LIA by setting f_1^R equal to f_2^R [6,23]. With ϕ_1^R - ϕ_2^R = π, the single LIA output becomes $S_B(t) = 2\alpha\Delta B(t)$; thus the N-$V$ diamond sensor functions as a magnetometer with a doubled contrast or zero-crossing slope. Conversely, the N-V diamond sensor acts a thermometer when $f_1^R = f_2^R$ but $\phi_1^R = \phi_2^R$, since $S_T(t) = 2\alpha\Delta D(t)$.

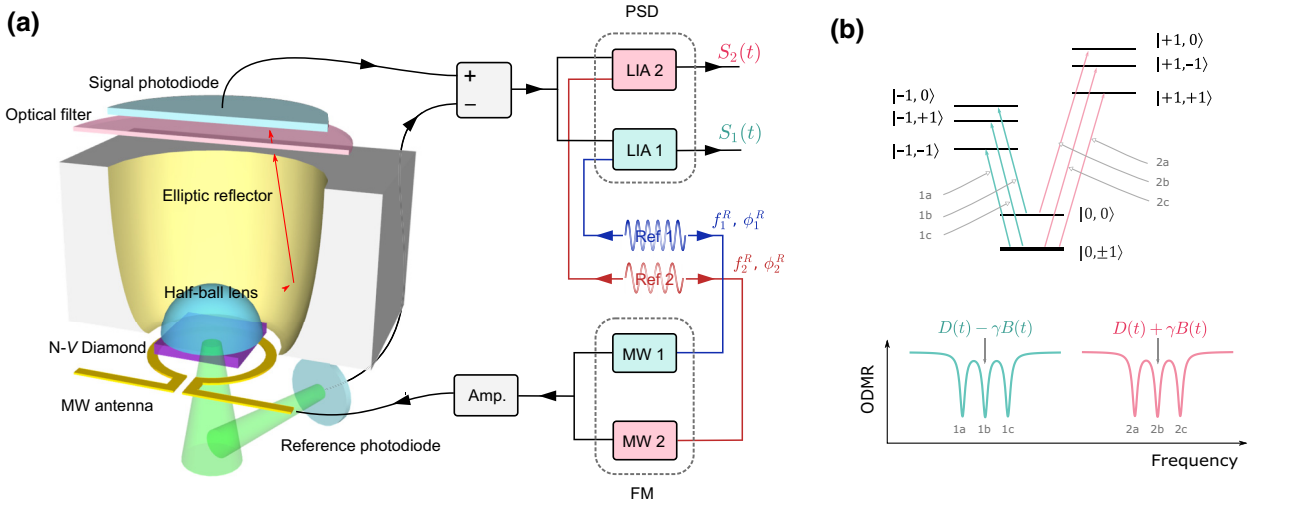

FIG. 1. (a) Configuration of the multiplexed N-V diamond sensor with signals driving and lock-in detection for dual-frequency driving. A half-ball lens on the top of the N-V diamond sample in combination with an elliptic reflector guides the fluorescence from N-V centers to the signal photodiode. The reference photodiode monitors the 532-nm pump beam (green) and is used to suppress laser-intensity fluctuations by subtracting the output of the reference photodiode from the signal photodiode using a balanced circuit. Reference signals Ref1 and Ref2 are fed into the microwave sources (MW1 and MW2) and the lock-in amplifiers (LIA1 and LIA2) for frequency modulation (FM) and phase-sensitive detection (PSD), respectively. The frequencies (f_1^R and f_2^R) and phases (ϕ_1^R and ϕ_2^R) of the reference signals (Ref1 and Ref2) for FM are controllable parameters for dual-frequency driving (described in the text). (b) Top: energy diagram of the N-V electronic spin coupled with a ^{14}N nuclear spin, indicating six transitions. Bottom: schematic N-V ODMR spectrum, indicating the six transition frequencies.

D. Effect of coherent population trapping

There are nine possible combinations of N-V hyperfine transitions that can be driven in the measurement schemes discussed in the present paper. Ideally, the pair of middle hyperfine lines, as indicated by green arrows in Fig. 2(a), would be used to make the measured ODMR line shape symmetric. We find, however, that such a combination should be excluded due to the diminished ODMR contrast caused by coherent population trapping (CPT) [28,29]. The need to exclude transitions impacted by CPT effects necessitates further analysis on the extracted magnetometry and thermometry signals to mitigate nonlinear effects [24]. A detailed analysis of CPT on N-V spin states with a cw microwave and a laser is beyond the scope of the present paper. Therefore, we give a brief phenomenological explanation, as follows. In Fig. 2(b), the two transitions indicated by green arrows can form a V-type level configuration, because the two excited states, $|-1,0\rangle$ and $|+1,0\rangle$, possess the same ^{14}N nuclear spin state, $m_I = 0$ with no hyperfine splitting. The two microwave signals, then, interact coherently and render a bright $|B\rangle$ and a dark $|D\rangle$ state on the N-V electronic spins, which are a linear superposition of $m_S = |+1\rangle$ and $|-1\rangle$ [29,30], as follows:

$$|B\rangle = \frac{1}{\sqrt{\Omega_+^2 + \Omega_-^2}}[\Omega_-|-1\rangle + \Omega_+|+1\rangle],$$
$$|D\rangle = \frac{1}{\sqrt{\Omega_+^2 + \Omega_-^2}}[\Omega_+|-1\rangle - \Omega_-|+1\rangle], \quad (3)$$

where Ω_+ and Ω_- are the associated Rabi frequencies of the N-V transitions. As there is irreversible decay from $|B\rangle$ to $|D\rangle$ due to spin relaxation, the population of the excited state is trapped in the dark state. This trapping process, however, competes with the decoherence in the excited states and the repolarization to $|0\rangle$, caused by the laser pumping. As Ω_- increases, the dark state becomes closer to $|-1\rangle$ since $|\langle -1|D\rangle|^2 = (\Omega_+^2/\Omega_+^2 + \Omega_-^2)$. As a result, the trapping is less affected by the laser-induced decoherence. This explanation is further supported by increased suppression of the ODMR contrast with an increased microwave power at f_+, as shown in Fig. 2(c). Thus, one needs to avoid CPT in order to take advantage of doubled contrast when using dual-frequency driving. For the results shown in Figs. 3 and 4, we adopt a MW pair indicated by the blue and yellow arrows in Figs. 2(a) and 2(b), which avoids a V-type configuration and CPT.

E. Multiplexed sensing of magnetic field and temperature

Figures 3(a) and 3(b) are example real-time traces of the outputs of LIA1 and LIA2, respectively. The digitized signals are then subtracted [Fig. 3(c)] and summed [Fig. 3(d)]. The subtracted signal manifests rapid variations, while the summed signal exhibits a relatively smoother and gradual increment. To verify that the subtracted signal measures magnetic field variation only, we apply a magnetic field modulation of amplitude 38.9 nT (rms) at 10 Hz for 3 s and find that the test field signal only appears on the subtracted

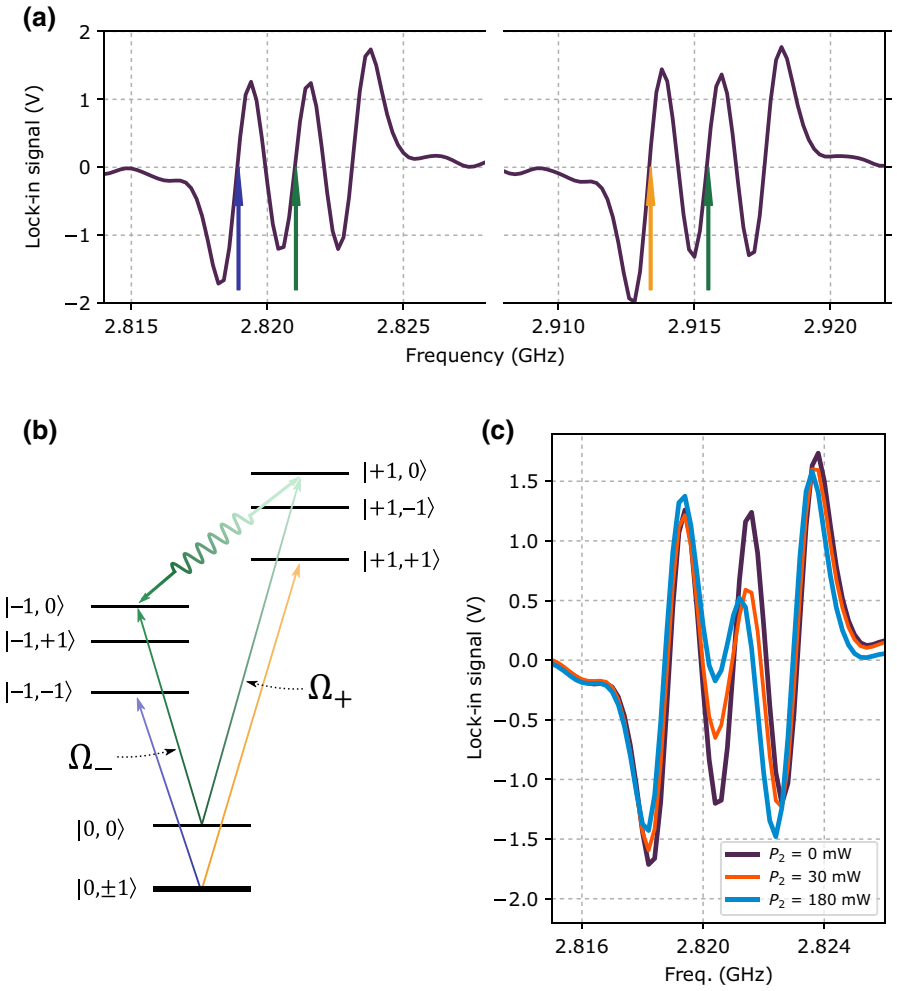

FIG. 2. (a) ODMR spectrum obtained by phase-sensitive detection using LIA, as outlined in main text. The colored arrows indicate the frequencies of the transitions represented in (b) with the same colors. (b) The transition pair (green) have Rabi frequencies of Ω_+ and Ω_- and form a V-type level configuration, which leads to coherent bright $|B\rangle$ and dark $|D\rangle$ states; in contrast, the other pair (blue, yellow) does not. (c) Coherent population trapping (CPT) involving $|B\rangle$ and $|D\rangle$ suppresses the ODMR contrast. The suppression becomes higher as the power of MW2 (P_2) increases.

time trace. The noticeable differences between Figs. 3(c) and 3(d) can be explained by a fluctuation of the ambient magnetic field at low frequency. To confirm that the summed signal interrogates the temperature, we measure the temperature of the N-V diamond sensor with a thermal sensor (PT100) mounted about 5 mm from the diamond on the sapphire plate (see Appendix and the Supplemental Material [24]) and correlate it with the summed signal as shown in Fig. 4(c). A linear correlation is obtained, with a slope that is used for the calibration of the vertical scale of the summed signal [Fig. 3(d)]. Similarly, Fig. 4(b) shows the signal obtained with a known magnetic field test signal of 1 μT (rms) and 10 Hz, applied for the calibration of the vertical scale of the subtracted signal [Fig. 3(c)].

F. Sensitivity

For the estimation of the magnetic field and temperature sensitivity, the output of LIA1 is fed into a FFT spectrum analyzer directly in order to bypass noise contributions during digitization. Here, the reference frequency f_1^R is set equal to f_2^R for operating N-V diamond as either a magnetometer or a thermometer, respectively. (Note that the data used in Fig. 4(a) is independent of that shown in Fig. 3.) The noise spectra in Fig. 4(a) contain the responses in both sensing modes to a test magnetic field signal at 10 Hz and about 1 μT amplitude on top of the observed noise floor. The noise spectrum of the N-V diamond magnetometry signal includes the main test-signal peak at 10 Hz and higher harmonics indicated by gray arrows; all these signals are greatly reduced in the N-V diamond thermometry signal, as expected. The power-line (60-Hz) noise is marked by the red arrow. The $1/f$ noise below about 4 Hz is suppressed in the N-V diamond thermometry signal compared to the N-V magnetometry signal, suggesting that the ambient environment contains pronounced low-frequency magnetic field fluctuations. The noise floor of the N-V diamond thermometer is also lower than that of the magnetometer for frequencies up to 100 Hz, which is again attributed to insensitivity to ambient magnetic fluctuations. When all the microwaves are turned off, the noise level decreases by about 3 dB. Given the measured strength of the test field in Fig. 4(b) and the measured slope in Fig. 4(c), the noise floors are converted into

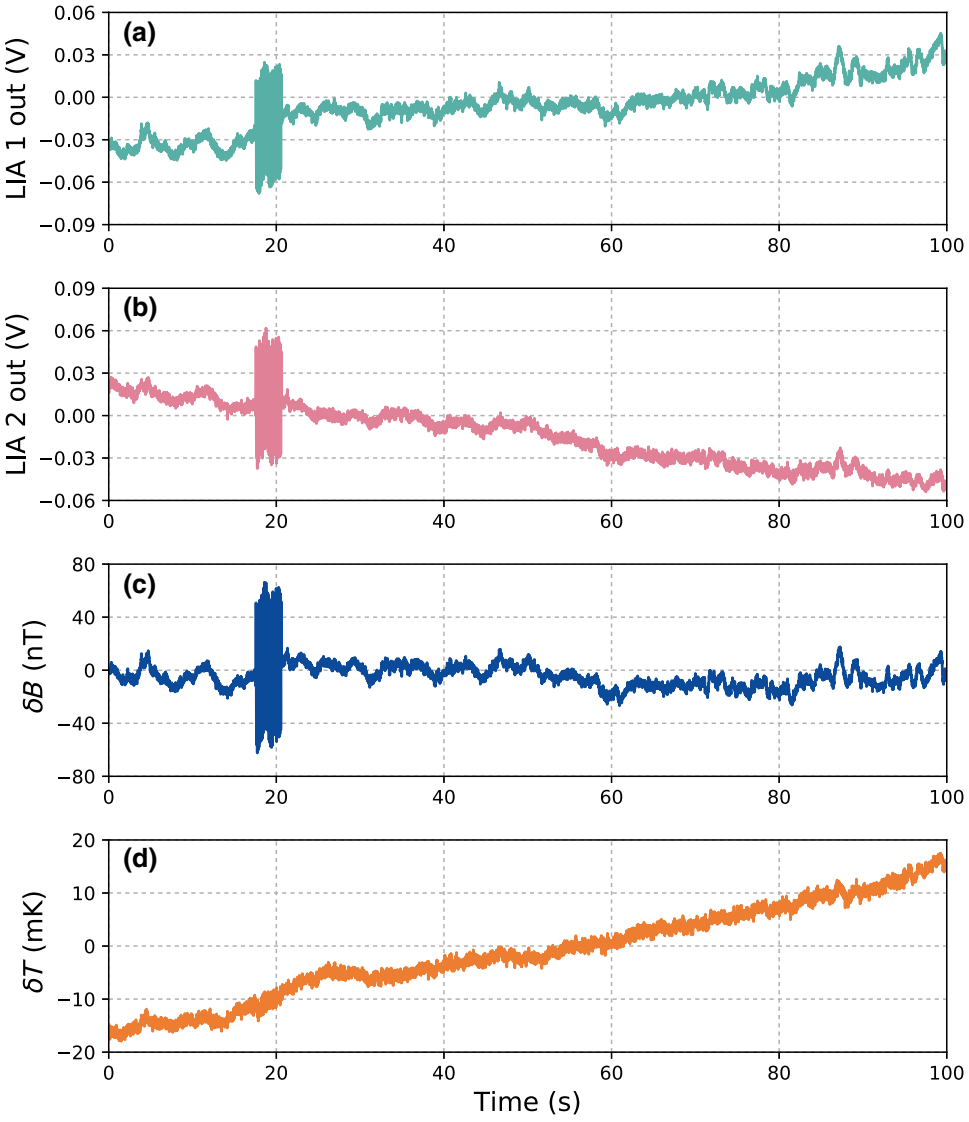

FIG. 3. (a),(b) Time traces of measured outputs for LIA1 and LIA2, as shown in Fig. 1(a). The summed and subtracted signals are shown in (c) and (d), respectively. A magnetic field test signal of 38.9 nT (rms) at 10 Hz is applied for 3 s, ending at about 20 s on the data shown here. The vertical axes of (c) and (d) are scaled according to the calibration shown in Figs. 4(b) and 4(c). The applied magnetic field is visible only in the summed signal, while the subtracted signal senses temperature variation.

sensitivities pf of 70 pT/Hz$^{1/2}$ and 25 μK/Hz$^{1/2}$ for the magnetometer and thermometer, respectively.

G. Isolation factor

In Fig. 4(a), the main peak at 10 Hz of the N-V thermometry signal is significantly reduced by about 34 dB, which we define as the isolation factor. We perform theoretical and numerical analyses in order to investigate the limitations of the isolation factor and the presence of higher harmonics [24]. We note three dominant effects: (1) off-axis magnetic field contributions in the Hamiltonian; (2) nonlinear effects due to the Lorentzian ODMR line shape; and (3) error in balancing the zero-crossing slopes. Our numerical analysis reveals that the nonlinear effect contributes only to the even harmonics (20 Hz, 40 Hz, etc.), while the balancing error can significantly reduce the isolation factor (10 Hz). We thus minimize the main peak intensity at 10 Hz in the N-V thermometry signal by tuning MW power and the relative phases of the lock-in amplifier (see further information below). When the balancing error is negligible, second-order terms in the Hamiltonian, involving the off-axis components B_x and B_y, should be considered to explain the isolation factor. We assume that the time-varying field from the test magnetic field at 10 Hz has off-axis component ΔB_x (with $\Delta B_y = 0$) and that $\Delta B_x < B_x$. Then, the variation of the N-V resonance frequencies Δf_+ and Δf_- can be expressed as [31]

$$\Delta f_{\pm} = \left(\frac{\partial f}{\partial T}\right)\Delta T \pm \frac{\gamma}{2\pi}\Delta B_z + \frac{3}{D}\left(\frac{\gamma}{2\pi}\right)^2 B_x \Delta B_x, \quad (4)$$

in which ΔT and ΔB_z represent the changes of temperature and magnetic field along N-V axis, respectively. The ${\Delta B_x}^2$ term is omitted since it is smaller than the $B_x \Delta B_x$ term. Equation (4) indicates that the off-axis magnetic field component can couple into the thermometry signal $S_T(t)$ through a second-order term, since $S_T(t) =$

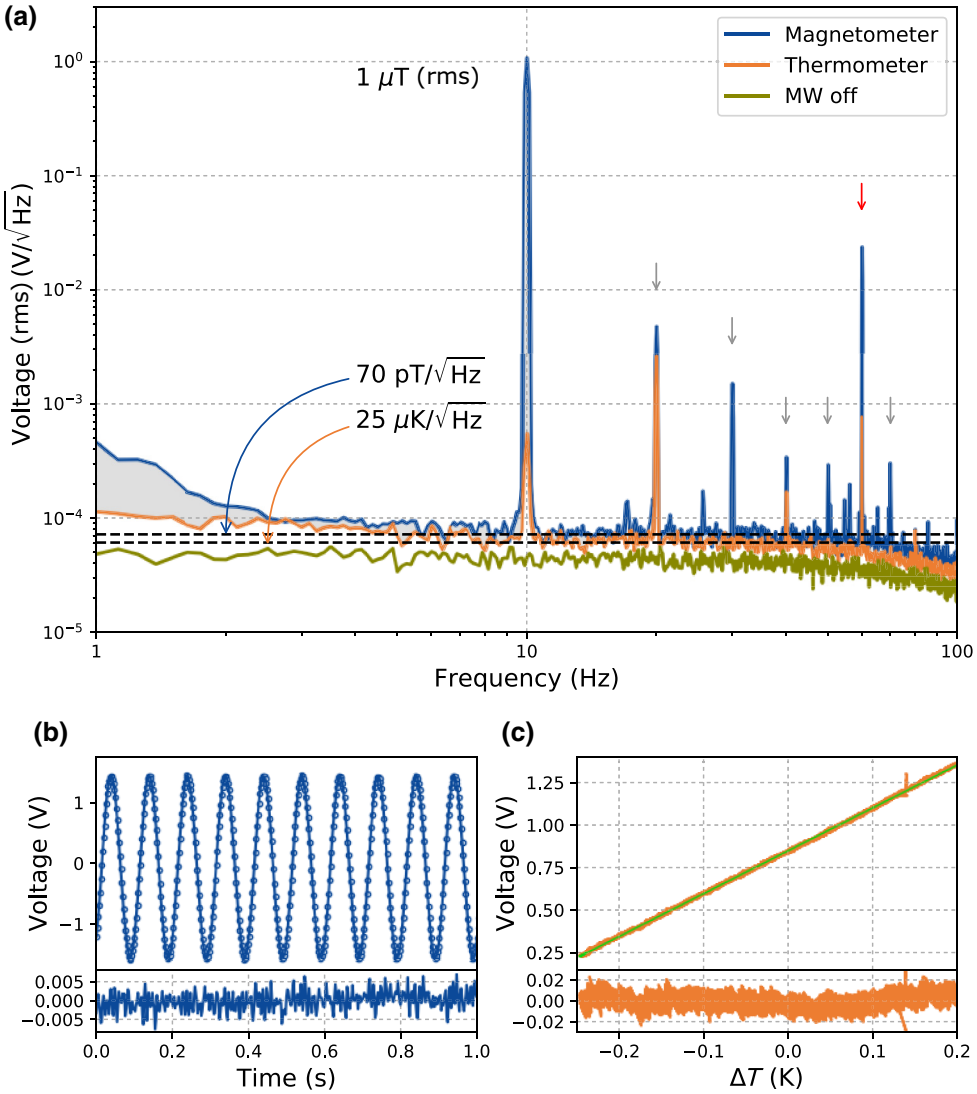

FIG. 4. (a) Noise spectra of the N-V diamond magnetometry and thermometry signals. The system noise is characterized without microwaves (MW off). A test magnetic field of 1 μT (rms) at 10 Hz is applied for estimating the isolation factor and for sensitivity calibration. When the N-V sensor functions as a thermometer, the signal due to the test field is reduced by about 34 dB. The peaks indicated by gray arrows are higher harmonics of the test field and the red arrow indicates power-line noise at 60 Hz. The gray area below about 4 Hz represents $1/f$ magnetic field noise. (b) The signal of the N-V magnetometer is recorded for 1 s in the presence of the test magnetic field (top panel). The amplitude obtained from numerical fitting is used for the magnetic sensitivity calibration. The residual error of the fitting is shown below (bottom panel). (c) The temperature of the N-V diamond (horizontal axis) is recorded with a PT100 sensor for over 2 h, in addition to the signal of the N-V thermometer (vertical axis). A linear response is obtained (top panel). The slope, estimated from linear fit (green line), is used for the temperature sensitivity calibration. The residual error is shown below (bottom panel). After calibration, the sensitivities of the N-V magnetometer and N-V thermometer are determined to be about 70 pT/$\sqrt{\text{Hz}}$ and 25 μK/$\sqrt{\text{Hz}}$, respectively.

$2\alpha[(\partial f/\partial T)\Delta T + (3/D)(\gamma/2\pi)^2 B_x \Delta B_x]$. The isolation factor ξ can then be obtained as

$$\xi = \frac{2\pi D \Delta B_z}{3\gamma B_x \Delta B_x}, \tag{5}$$

which reveals that reducing the off-axis components (both B_x and ΔB_x) is crucial in enhancing the isolation factor. Given the experimental configuration that we employ, $\Delta B_z = 1$ μT (rms) and $\Delta B_x = \sqrt{2}$ μT (rms) (see the Supplemental Material [24]). From the experimentally obtained value of $\xi = 2511$ (34 dB), the off-axis field B_x is estimated to be 8.37 μT, corresponding to a misalignment angle of 0.3° of the (static) magnetic field from the target N-V axis in the diamond sensor.

III. DISCUSSION

In the spectrum of the N-V thermometer in Fig. 4(a), peaks are observed at even harmonic, of the signal frequency (10 Hz). We conduct our numerical simulations [24] with an assumption that the N-V spin resonances, measured by ODMR, are well approximated by a Lorentzian line shape; and without including second-order terms in Eq. (4), to isolate the effects of nonlinear line shapes from higher order terms in the Hamiltonian. Our numerical simulations attribute the observed N-V thermometer higher harmonic peaks to the nonlinearity in the zero-crossing slope of the derivative of the Lorentzian lines when shifted from the points of maximum slope. According to the simulations, dual-frequency driving for the N-V thermometer effectively eliminates odd harmonic peaks, leaving only even harmonics (see the Supplemental Material [24]). For the N-V magnetometry signal, the nonlinear line-shape simulation shows that only odd harmonic peaks appear given the measurement protocol, which is inconsistent with the 20-Hz and other even harmonic magnetometry peaks in the observed spectrum shown in Fig. 4(a). We extend the initial numerical simulations by including imperfections in matching the two zero-crossing slopes of f_+ and f_- to explain additional even harmonics in the magnetometry spectrum. The experimental data presented in Fig. 4(a) combined with the numerical simulations elucidate how important it is to match the slopes of f_+ and f_- for optimized dual-frequency driving. Since the zero-crossing slopes depend significantly on several experimental parameters including MW power, laser polarization, and diamond properties, it is challenging in practice to achieve identical slopes for a N-V ensemble. According to the simulations, a mismatch of 1%–5% is sufficient to produce a second-harmonic peak in the N-V magnetometry signal similar to that observed in the experiment. For the case of the N-V thermometry signal, we experimentally minimize the spectral peak magnitude at 10 Hz by tuning the phase ϕ_1^R and ϕ_2^R of the reference signals, which provides one method to counteract experimental mismatches and imperfections. In future experiments, the effect of nonlinearities could be reduced through fast feedback on the MW center frequency to stay in the linear regime as much as possible [32].

The isolation factor (Eq. (5)) could be used to achieve a precise alignment of the magnetic field to the N-V axis. According to Eq. (5), the off-axis field parallel to the test field B_x should be minimized for a higher isolation factor. To verify that both B_x and B_y are minimized, one needs an additional perpendicular test field. Thus, with the two test fields in different orientations, the N-V thermometer spectral peak magnitude at the frequency of the test field indicates the field alignment. Other off-axis field-dependent phenomena have been reported for N-Vs, such as nuclear spin polarization at excited-state level anticrossing [33] and a decrease in photoluminescence intensity [34]. Both may also be used for the alignment of the magnetic field. However, the former effect occurs only at a specific field near 50 mT and the latter requires a relatively strong field, larger than about 10 mT. Equation (5) is expected to be valid at much weaker magnetic fields, as it relies on a second-order approximation. Thus, the isolation factor presented here could be a useful metric to aid the alignment of a magnetic fields of a few millitesla.

Of the four crystal axes in diamond, N-V centers along the [111] orientation are exploited in the present work. As previously demonstrated, one can overlap the observed ODMR spectra from all four the N-V orientations in an ensemble by applying an external magnetic field along the [100] orientation, and thereby maximizing the ODMR contrast and enhancing magnetometer and thermometer sensitivity [1]. N-Vs that are not aligned to the external magnetic field have an issue of asymmetry in the N-V resonance frequency shift due to external magnetic field variations, $\partial f/\partial B$; the ODMR peak at the lower MW frequency is less sensitive to magnetic fields than that at the higher MW frequency [24]. This asymmetry stems from the nonlinear response to the off-axis magnetic field in the presence of the zero-field splitting. The discrepancy in $\partial f/\partial B$ causes the isolation factor to deteriorate, as the first-order terms (ΔB_z) in Eq. (4) cannot be cancelled with each other in the thermometry signal $S_T(t)$.

In Fig. 4(a), the noise floor for magnetically insensitive operation, when MW1 and MW2 are off, is about 41 pT/$\sqrt{\text{Hz}}$. The shot-noise limits obtained from Eqs. (1) and (2) are 13.5 pT/$\sqrt{\text{Hz}}$ for the N-V magnetometer and 5μK/$\sqrt{\text{Hz}}$ for the N-V thermometer, values that are approximately a factor of about 5 time more sensitive than the experimental results. This discrepancy is attributed to incomplete cancellation of noise from the pumping laser, as well as additional noise when MW1 and MW2 are applied due to the microwave amplifier. In the present study, the illumination spot of the pumping laser on the diamond has a diameter of about 0.5 mm. Since the thickness of the diamond is 0.3 mm, the effective N-V ensemble sensing volume is approximately 6×10^7 μm^3 and the volume-normalized magnetic field sensitivity for a 10 Hz signal frequency is about 542 nT $\times$ $\mu\text{m}^{3/2}/\sqrt{\text{Hz}}$. We note that increasing the laser spot size causes the volume-normalized sensitivity to deteriorate significantly, consistent with there being spatial inhomogeneity across the N-V ensemble of key parameters such as local strain, concentration of N-Vs, N_S^0, and other paramagnetic impurities, external magnetic field, MW power, etc.

IV. CONCLUSION

In this work, we demonstrate real-time multiplexed sensing of two physical quantities, magnetic field and temperature, using an ensemble of N-V centers in

diamond. Sensitivities of 70 pT/$\sqrt{\text{Hz}}$ and 25 μK/$\sqrt{\text{Hz}}$ are achieved for the magnetic field and the temperature, respectively, with good isolation of about 34 dB in temperature against the magnetic field during simultaneous measurements. We develop a model of the experimental parameters and their effect on the N-V measurements to help characterize and improve the isolation factor. This study is motivated by the need to eliminate N-V signal drifts caused by ambient thermal variation. Such variations can come from many sources, e.g., thermal radiation, conduction through physical contacts, and convection of surrounding air flows. Thus, one must isolate thermal effects for reliable operation of an N-V diamond magnetometer and vice versa for an N-V thermometer. Dual-frequency driving makes simultaneous measurement of both quantities feasible, with straightforward implementation. Our method may extend N-V diamond sensing applications into a wider variety of fields. These may include *operando* [35] or *in vitro* [36] monitoring, in which a chemical reaction occurs actively and generates charge currents with heat production. Additionally, the source of a magnetic field can be highly temperature dependent, as is the case for magnetic nanoparticles having Curie temperatures near room temperature [37]. In such conditions, multiplexed N-V diamond sensors will provide more accurate analysis by separating the effects of the magnetic field and the temperature.

ACKNOWLEDGMENTS

This research was supported by the Korea Research Institute of Standards and Science (Grant No. GP2021-0010) and by a Institute of Information and Communications Technology (IITP) Planning & Evaluation grant funded by the Korea government (MSIT) (Grant No. 2019-000296). The efforts of the University of Maryland Quantum Technology Center personnel (C.A.H., M.J.T., and R.L.W.) were supported by the U.S. Army Research Laboratory Maryland-ARL Quantum Partnership (MAQP) program under Contract No. W911NF-19-2-0181.

APPENDIX: EXPERIMENTAL METHODS

1. N-V diamond

The N-V diamond is a general-grade HPHT crystal (Element Six). The dimensions of the diamond are $3 \times 3 \times 0.3$ mm^3 and the initial N_S^0 concentration is approximately 30 ppm. To increase the concentration of N-V centers, the diamond is electron irradiated (1 MeV and 1×10^{19} e/cm^2) and annealed in vacuum at 950 °C for 4 h. Post-treatment, the N-V concentration and remnant N_S^0 are measured using EPR and FTIR to be about 0.5 ppm (conversion efficiency 1.7%) and 1.3 ppm, respectively [24,38,39].

2. Optical system

The 532-nm pump laser (Millennia eV, 10 W) has an output power of 600 mW. The pump laser path is split by using a polarizing beam splitter and a half-wave plate. The split path enters into the reference photodiode (Hamamatsu, S1337), monitoring the pump laser power. The fluorescence from the N-V ensemble is collected by the signal photodiode (Hamamatsu, S1337). The photoinduced current is typically 11 mA. The reference and signal photodiodes are interconnected through a home-made balanced circuit, the output voltage of which is proportional to the difference between the photoinduced currents out of the reference and the signal photodiodes. Such balanced detection efficiently cancels the common noise from the pump laser. The power split of the pump laser is adjusted to balance the photoinduced currents on both photodiodes, with about 400 mW of green pump typically exciting the N-V ensemble. The pump laser is focused onto the N-V ensemble through a lens (f = 100 mm) with a typical spot size of 0.5 mm; and its optical polarization is adjusted to maximize the ODMR contrast from N-V centers along the [111] orientation. The half-ball lens is commercially available (Edmund) and made of a high-refractive-index material (S-LAH79, n = 1.987 at 700 nm). The elliptic reflector is manufactured via high-precision machining (Nanoform L 1000) of an aluminum block. The surface roughness is typically less than 5 nm. The half-ball lens is glued to the N-V diamond.

3. Electronic system

Two microwave sources (SG380) receive reference signals for the frequency modulation of MW1 and MW2. The reference signals are generated by a two-channel function generator (Agilent 33522A). For multiplexed sensing, the frequencies of the references f_1^R and f_2^R are set to 5 kHz and 7 kHz, respectively. A sinusoidal waveform is used for the reference signals and the modulation depth is 0.55 MHz for both f_1^R and f_2^R. The frequency-modulated signals MW1 and MW2 are combined and put into a power amplifier (Minicircuit, 16 W). The output powers of MW1 and MW2 are typically 30 mW. Through a microstrip line on a printed circuit board, the amplified microwave signal is guided to an Ω-shaped antenna with a diameter of 7 mm and terminated with a 50 Ω load. The antenna is mounted below a sapphire glass plate, upon which the N-V diamond is positioned inside the elliptic reflector. A permanent magnet (5 cm × 5 cm × 2.5 cm) produces an external magnetic field of about 1.6 mT at the position of the pump laser spot on the N-V diamond. The permanent magnet is positioned on a combination of vertical and rotational stages, which allows careful alignment of the magnetic field along the [111] orientation of the diamond. A Helmholtz coil, of diameter 20 cm, is used to produce test magnetic fields at 10 Hz. The test magnetic field

magnitude (rms) is calibrated with a flux-gate sensor. The sensitivity and the time constant of the two lock-in amplifiers (SR860) are set to 2 mV and 1 ms, respectively. A three-channel data-acquisition device is used for digitizing the N-V fluorescence time-trace signals with a device (NI-4461) of 24-bit resolution and a sampling rate of 1 kS/s. The first and second channels are connected to the outputs of LIA1 and LIA2, respectively. The third channel measures the voltages across the PT100 temperature sensor via the four-probe method. An external source applies a current of 10 mA through the PT100 sensor. The resistance of the PT100 sensor is calibrated as a function of temperature prior to the N-V measurements.

4. Data processing

For MW1 and MW2 used for dual-frequency driving, the power and modulation depths are adjusted not only for optimizing N-V sensitivity but also for balancing nearly the same signal in the two detection channels in the presence of the test signal. For a high isolation factor during multiplexed sensing, such balancing is required but imperfect, due to the difficulty in matching two large signals with a high degree of precision. Thus, we perform an additional process; the digitized time-trace signals (S_1 and S_2) from LIA1 and LIA2 are summed (S_T) and subtracted (S_B) as follows:

$$\begin{aligned} S_T &= \sqrt{2}\left[\cos\left(\frac{\pi}{4}+\epsilon\right)S_1 + \sin\left(\frac{\pi}{4}+\epsilon\right)S_2\right], \\ S_B &= \sqrt{2}\left[\cos\left(\frac{\pi}{4}+\epsilon\right)S_1 - \sin\left(\frac{\pi}{4}+\epsilon\right)S_2\right]. \end{aligned} \tag{A1}$$

The phase ϵ is digitally tuned with a precision of 0.01° to minimize the intensity of the test signal on S_T. Typically, ϵ varies within $\pm 1.5^\circ$.

[1] J. F. Barry, M. J. Turner, J. M. Schloss, D. R. Glenn, Y. Song, M. D. Lukin, H. Park, and R. L. Walsworth, Optical magnetic detection of single-neuron action potentials using quantum defects in diamond, Proc. Natl. Acad. Sci. **113**, 14133 (2016).

[2] S. Ahmadi, H. A. R. El-Ella, J. O. B. Hansen, A. Huck, and U. L. Andersen, Pump-Enhanced Continuous-Wave Magnetometry Using Nitrogen-Vacancy Ensembles, Phys. Rev. Appl. **8**, 034001 (2017).

[3] G. Chatzidrosos, A. Wickenbrock, L. Bougas, N. Leefer, T. Wu, K. Jensen, Y. Dumeige, and D. Budker, Miniature Cavity-Enhanced Diamond Magnetometer, Phys. Rev. Appl. **8**, 044019 (2017).

[4] J. M. Schloss, J. F. Barry, M. J. Turner, and R. L. Walsworth, Simultaneous Broadband Vector Magnetometry Using Solid-State Spins, Phys. Rev. Appl. **10**, 034044 (2018).

[5] H. Zheng, J. Xu, G. Z. Iwata, T. Lenz, J. Michl, B. Yavkin, K. Nakamura, H. Sumiya, T. Ohshima, J. Isoya, J. Wrachtrup, A. Wickenbrock, and D. Budker, Zero-Field Magnetometry Based on Nitrogen-Vacancy Ensembles in Diamond, Phys. Rev. Appl. **11**, 064068 (2019).

[6] I. Fescenko, A. Jarmola, I. Savukov, P. Kehayias, J. Smits, J. Damron, N. Ristoff, N. Mosavian, and V. M. Acosta, Diamond magnetometer enhanced by ferrite flux concentrators, Phys. Rev. Res. **2**, 023394 (2020).

[7] J. L. Webb, L. Troise, N. W. Hansen, C. Olsson, A. M. Wojciechowski, J. Achard, O. Brinza, R. Staacke, M. Kieschnick, J. Meijer, A. Thielscher, J.-F. Perrier, K. Berg-Sørensen, A. Huck, and U. L. Andersen, Detection of biological signals from a live mammalian muscle using an early stage diamond quantum sensor, Sci. Rep. **11**, 2412 (2021).

[8] J. F. Barry, J. M. Schloss, E. Bauch, M. J. Turner, C. A. Hart, L. M. Pham, and R. L. Walsworth, Sensitivity optimization for NV-diamond magnetometry, Rev. Mod. Phys. **92**, 015004 (2020).

[9] M. W. Doherty, F. Dolde, H. Fedder, F. Jelezko, J. Wrachtrup, N. B. Manson, and L. C. L. Hollenberg, Theory of the ground-state spin of the nv^- center in diamond, Phys. Rev. B **85**, 205203 (2012).

[10] V. M. Acosta, E. Bauch, M. P. Ledbetter, A. Waxman, L.-S. Bouchard, and D. Budker, Temperature Dependence of the Nitrogen-Vacancy Magnetic Resonance in Diamond, Phys. Rev. Lett. **104**, 070801 (2010).

[11] F. Dolde, H. Fedder, M. W. Doherty, T. Nöbauer, F. Rempp, G. Balasubramanian, T. Wolf, F. Reinhard, L. C. L. Hollenberg, F. Jelezko, and J. Wrachtrup, Electric-field sensing using single diamond spins, Nat. Phys. **7**, 459 (2011).

[12] M. E. Trusheim and D. Englund, Wide-field strain imaging with preferentially aligned nitrogen-vacancy centers in polycrystalline diamond, New J. Phys. **18**, 123023 (2016).

[13] M. W. Doherty, V. V. Struzhkin, D. A. Simpson, L. P. McGuinness, Y. Meng, A. Stacey, T. J. Karle, R. J. Hemley, N. B. Manson, L. C. L. Hollenberg, and S. Prawer, Electronic Properties and Metrology Applications of the Diamond nv^- Center under Pressure, Phys. Rev. Lett. **112**, 047601 (2014).

[14] H. J. Mamin, M. H. Sherwood, M. Kim, C. T. Rettner, K. Ohno, D. D. Awschalom, and D. Rugar, Multipulse Double-Quantum Magnetometry with Near-Surface Nitrogen-Vacancy Centers, Phys. Rev. Lett. **113**, 030803 (2014).

[15] Erik Bauch, Connor A. Hart, Jennifer M. Schloss, Matthew J. Turner, John F. Barry, Pauli Kehayias, Swati Singh, and Ronald L. Walsworth, Ultralong Dephasing Times in Solid-State Spin Ensembles via Quantum Control, Phys. Rev. X **8**, 031025 (2018).

[16] P. Neumann, I. Jakobi, F. Dolde, C. Burk, R. Reuter, G. Waldherr, J. Honert, T. Wolf, A. Brunner, J. H. Shim, D. Suter, H. Sumiya, J. Isoya, and J. Wrachtrup, High-precision nanoscale temperature sensing using single defects in diamond, Nano Lett. **13**, 2738 (2013).

[17] G. Kucsko, P. C. Maurer, N. Y. Yao, M. Kubo, H. J. Noh, P. K. Lo, H. Park, and M. D. Lukin, Nanometre-scale thermometry in a living cell, Nature **500**, 54 (2013).

[18] D. M. Toyli, C. F. d. l. Casas, D. J. Christle, V. V. Dobrovitski, and D. D. Awschalom, Fluorescence thermometry

enhanced by the quantum coherence of single spins in diamond, Proceedings of the National Academy of Sciences **110**, 8417 (2013).

[19] Mason C. Marshall, Reza Ebadi, Connor Hart, Matthew J. Turner, Mark J.H. Ku, David F. Phillips, and Ronald L. Walsworth, High-precision mapping of diamond crystal strain using quantum interferometry, arXiv:2108.00304 [quant-ph] (2021).

[20] H. Clevenson, M. E. Trusheim, C. Teale, T. Schröder, D. Braje, and D. Englund, Broadband magnetometry and temperature sensing with a light-trapping diamond waveguide, Nat. Phys. **11**, 393 (2015).

[21] H. Clevenson, L. M. Pham, C. Teale, K. Johnson, D. Englund, and D. Braje, Robust high-dynamic-range vector magnetometry with nitrogen-vacancy centers in diamond, Appl. Phys. Lett. **112**, 252406 (2018).

[22] Y. Hatano, J. Shin, D. Nishitani, H. Iwatsuka, Y. Masuyama, H. Sugiyama, M. Ishii, S. Onoda, T. Ohshima, K. Arai, T. Iwasaki, and M. Hatano, Simultaneous thermometry and magnetometry using a fiber-coupled quantum diamond sensor, Appl. Phys. Lett. **118**, 034001 (2021).

[23] A. M. Wojciechowski, M. Karadas, C. Osterkamp, S. Jankuhn, J. Meijer, F. Jelezko, A. Huck, and U. L. Andersen, Precision temperature sensing in the presence of magnetic field noise and vice-versa using nitrogen-vacancy centers in diamond, Appl. Phys. Lett. **113**, 013502 (2018).

[24] See the Supplemental Material at http://link.aps.org/supplemental/10.1103/PhysRevApplied.17.014009 for details of the simulation results of the photon collection and nonlinear response, etc.

[25] P. C. D. Hobbs, *Building Electro-Optical Systems* (John Wiley & Sons, Inc., Hoboken, New Jersey, 2009).

[26] A. M. Edmonds, C. A. Hart, M. J. Turner, P.-O. Colard, J. M. Schloss, K. Olsson, R. Trubko, M. L. Markham, A. Rathmill, B. Horne-Smith, W. Lew, A. Manickam, S. Bruce, P. G. Kaup, J. C. Russo, M. J. DiMario, J. T. South, J. T. Hansen, D. J. Twitchen, and R. Walsworth, Characterisation of CVD diamond with high concentrations of nitrogen for magnetic-field sensing applications, Mater. Quantum Technol. **1**, 025001 (2021).

[27] E. V. Levine, M. J. Turner, P. Kehayias, C. A. Hart, N. Langellier, R. Trubko, D. R. Glenn, R. R. Fu, and R. L. Walsworth, Principles and techniques of the quantum diamond microscope, Nanophotonics **8**, 1945 (2019).

[28] P. Kehayias, M. Mrózek, V. M. Acosta, A. Jarmola, D. S. Rudnicki, R. Folman, W. Gawlik, and D. Budker, Microwave saturation spectroscopy of nitrogen-vacancy ensembles in diamond, Phys. Rev. B **89**, 245202 (2014).

[29] P. Jamonneau, G. Hétet, A. Dréau, J.-F. Roch, and V. Jacques, Coherent Population Trapping of a Single Nuclear Spin under Ambient Conditions, Phys. Rev. Lett. **116**, 043603 (2016).

[30] J. H. Shim, B. Novak, I. Niemeyer, F. D. Brandao, and D. Suter, Characterization of hyperfine interaction between single electron and single nuclear spins in diamond assisted by quantum beat from the nuclear spin, arxiv:1307.0257 (2013).

[31] M. J. Turner, N. Langellier, R. Bainbridge, D. Walters, S. Meesala, T. M. Babinec, P. Kehayias, A. Yacoby, E. Hu, M. Lončar, R. L. Walsworth, and E. V. Levine, Magnetic Field Fingerprinting of Integrated-Circuit Activity with a Quantum Diamond Microscope, Phys. Rev. Appl. **14**, 014097 (2020).

[32] H. Clevenson, L. M. Pham, C. Teale, K. Johnson, and D. Englund, Robust high-dynamic-range vector magnetometry with nitrogen-vacancy centers in diamond, Appl. Phys. Lett. **112**, 252406 (2018).

[33] V. Jacques, P. Neumann, J. Beck, M. Markham, D. Twitchen, J. Meijer, F. Kaiser, G. Balasubramanian, F. Jelezko, and J. Wrachtrup, Dynamic Polarization of Single Nuclear Spins by Optical Pumping of Nitrogen-Vacancy Color Centers in Diamond at Room Temperature, Phys. Rev. Lett. **102**, 057403 (2009).

[34] J.-P. Tetienne, L. Rondin, P. Spinicelli, M. Chipaux, T. Debuisschert, J.-F. Roch, and V. Jacques, Magnetic-field-dependent photodynamics of single NV defects in diamond: An application to qualitative all-optical magnetic imaging, New J. Phys. **14**, 103033 (2012).

[35] J. Huang, L. Albero Blanquer, J. Bonefacino, E. R. Logan, D. Alves Dalla Corte, C. Delacourt, B. M. Gallant, S. T. Boles, J. R. Dahn, H.-Y. Tam, and J.-M. Tarascon, *Operando* decoding of chemical and thermal events in commercial Na(Li)-ion cells via optical sensors, Nat. Energy **5**, 674 (2020).

[36] J. Choi, H. Zhou, R. Landig, H.-Y. Wu, X. Yu, S. E. Von Stetina, G. Kucsko, S. E. Mango, D. J. Needleman, A. D. T. Samuel, P. C. Maurer, H. Park, and M. D. Lukin, Probing and manipulating embryogenesis via nanoscale thermometry and temperature control, Proc. Natl. Acad. Sci. **117**, 14636 (2020).

[37] N. Wang, G.-Q. Liu, W.-H. Leong, H. Zeng, X. Feng, S.-H. Li, F. Dolde, H. Fedder, J. Wrachtrup, X.-D. Cui, S. Yang, Q. Li, and R.-B. Liu, Magnetic Criticality Enhanced Hybrid Nanodiamond Thermometer under Ambient Conditions, Phys. Rev. X **8**, 011042 (2018).

[38] D. F. Howarth, J. A. Weil, and Z. Zimpel, Generalization of the lineshape useful in magnetic resonance spectroscopy, J. Magnetic Resonance **161**, 215 (2003).

[39] V. M. Acosta, E. Bauch, M. P. Ledbetter, C. Santori, K.-M. C. Fu, P. E. Barclay, R. G. Beausoleil, H. Linget, J. F. Roch, F. Treussart, S. Chemerisov, W. Gawlik, and D. Budker, Diamonds with a high density of nitrogen-vacancy centers for magnetometry applications, Phys. Rev. B **80**, 115202 (2009).